

## Article

# Synthesis of Sodium Cobalt Fluoride/Reduced Graphene Oxide (NaCoF<sub>3</sub>/rGO) Nanocomposites and Investigation of Their Electrochemical Properties as Cathodes for Li-Ion Batteries

Jiwoong Oh <sup>1,†</sup>, Jooyoung Jang <sup>1,†</sup>, Eunho Lim <sup>2,\*</sup>, Changshin Jo <sup>1,\*</sup>  and Jinyoung Chun <sup>3,\*</sup> 

<sup>1</sup> School of Chemical Engineering and Materials Science, Chung-Ang University (CAU), 84 Heukseok-ro, Dongjakgu, Seoul 06974, Korea; shanall@cau.ac.kr (J.O.); wndud2362@cau.ac.kr (J.J.)

<sup>2</sup> Chemical & Process Technology Division, Korea Research Institute of Chemical Technology (KRICT), 141 Gajeongro, Daejeon 34114, Korea

<sup>3</sup> Energy and Environmental Division, Korea Institute of Ceramic Engineering and Technology (KICET), Jinju, Gyeongnam 52851, Korea

\* Correspondence: eunholim@kRICT.re.kr (E.L.); changshin@cau.ac.kr (C.J.); jchun@kicet.re.kr (J.C.)

† These authors contributed equally to this work.

**Abstract:** In this study, sodium cobalt fluoride (NaCoF<sub>3</sub>)/reduced graphene oxide (NCF/rGO) nanocomposites were fabricated through a simple one-pot solvothermal process and their electrochemical performance as cathodes for Li-ion batteries (LIBs) was investigated. The NCF nanoclusters (NCs) on the composites (300–500 nm in size) were formed by the assembly of primary nanoparticles (~20 nm), which were then incorporated on the surface of rGO. This morphology provided NCF NCs with a large surface area for efficient ion diffusion and also allowed for close contact with the conductive matrix to promote rapid electron transfer. As a cathode for LIBs, the NCF/rGO electrode achieved a high reversible capacity of 465 mAh·g<sup>-1</sup> at 20 mA·g<sup>-1</sup> via the conversion reaction, and this enhancement represented more than five times the reversible capacity of the bare NCF electrode. Additionally, the NCF/rGO electrode exhibited both better specific capacity and cyclability within the current density testing range (from 20 to 200 mA·g<sup>-1</sup>), compared with those of the bare NCF electrode.

**Keywords:** sodium cobalt fluoride; reduced graphene oxide; nanocomposites; solvothermal synthesis; Li-ion batteries; high-capacity cathodes



**Citation:** Oh, J.; Jang, J.; Lim, E.; Jo, C.; Chun, J. Synthesis of Sodium Cobalt Fluoride/Reduced Graphene Oxide (NaCoF<sub>3</sub>/rGO) Nanocomposites and Investigation of Their Electrochemical Properties as Cathodes for Li-Ion Batteries. *Materials* **2021**, *14*, 547. <https://doi.org/10.3390/ma14030547>

Academic Editor: Dimitra Vernardou

Received: 8 January 2021

Accepted: 21 January 2021

Published: 24 January 2021

**Publisher's Note:** MDPI stays neutral with regard to jurisdictional claims in published maps and institutional affiliations.



**Copyright:** © 2021 by the authors. Licensee MDPI, Basel, Switzerland. This article is an open access article distributed under the terms and conditions of the Creative Commons Attribution (CC BY) license (<https://creativecommons.org/licenses/by/4.0/>).

## 1. Introduction

In the modern world, Li-ion batteries (LIBs) are essential energy storage devices. Due to the growing need for electric vehicles and energy storage systems, the demand for advanced LIBs has increased significantly in recent years. Accordingly, several studies on cathode materials [1–3], anode materials [4–6], separators [7,8], electrolytes [9,10], and other cell components [11] have been conducted, with a focus on manufacturing high-performance LIBs.

Intercalation materials such as LiCoO<sub>2</sub> (LCO) and LiNi<sub>x</sub>Mn<sub>y</sub>Co<sub>z</sub>O<sub>2</sub> (NMC) are actively used as cathode materials in commercial LIBs. They can promote highly reversible charge/discharge processes over stable cathode potential ranges. However, their Li<sup>+</sup> storage capacity needs to be enhanced for the development of next-generation battery systems. Though LCO has demonstrated good cyclic stability in small-sized commercial LIBs, only about half of the theoretical capacity (274 mAh·g<sup>-1</sup>) is utilized owing to the structural strain [12]. Similarly, NMC has insufficient capacity for next-generation high-energy vehicle applications, even though it exhibits stable operating voltage and a good electrical conductivity (10<sup>-5</sup> S·cm<sup>-1</sup>) [13]. To achieve high energy density, high capacity or wide reaction potential cathode materials are required. However, intercalation-based materials have intrinsically low reversible capacities owing to the limited space available for Li<sup>+</sup>

insertion into the materials. Therefore, to improve the energy density of LIBs, conversion reaction-based cells are considered.

Conversion materials are based on utilizing the multiple electrons that are present in the oxidation state of transition metals in metal-anion compounds ( $M_aX_b$ ; M: transition metal such as Fe, Cu, and Co. X: anion such as O, F, S, and N), through a conversion reaction [14,15]. For cathode applications, studies on  $Fe_aX_b$  compounds have been reported extensively [16–19], but  $Co_aX_b$  compounds have been barely studied.  $Co_aX_b$  compounds can be converted into hydride, sulfide, nitride, and fluoride forms [20]. Considering that cathode materials should have a high reaction voltage, the ionicity of the M-X bond must be increased to obtain higher output voltages [21]. Among the various  $Co_aX_b$  compounds, only fluoride is suitable as a cathode material because its ionicity is significantly higher than that of the other compounds.

Sodium metal fluoride ( $NaMF_3$ ) which has large theoretical capacities and a large voltage window are promising cathode materials because they are thermodynamically stable under standard conditions, in contrast to  $LiMF_3$  [22]. Sodium cobalt fluoride,  $NaCoF_3$  (NCF), has a theoretical capacity of  $578 \text{ mAh}\cdot\text{g}^{-1}$  in the reaction where 3  $Li^+$  ions are involved ( $NaCoF_3 \leftrightarrow Na^+ + CoF_3$ ,  $CoF_3 + 3Li^+ + 3e^- \leftrightarrow Co + 3LiF$ ) and  $385 \text{ mAh}\cdot\text{g}^{-1}$  in the reaction where it reacts with 2  $Li^+$  ions ( $NaCoF_3 + 2Li^+ + 2e^- \leftrightarrow NaF + Co + 2LiF$ ). Although only two  $Li^+$  ions react in the latter case, the capacity is twice the capacity that is achieved with intercalation materials (i.e., LCO and NMC). However, several problems are associated with NCF, which include: (i) they have insulating properties due to their large bandgap. This low electrical conductivity can result in uneven distribution and slow diffusion of electrons in the electrode [23]; (ii) the metal formed by the conversion process should be reoxidized during the reverse process [24,25]. However, in the bulk state of some metal fluoride, significant separation of the metal and LiF occurs, resulting in a difficult reoxidation process [19]. For these reasons, only  $NaFeF_3$  has shown limited capacity ( $225 \text{ mAh}\cdot\text{g}^{-1}$ ) in sodium-ion battery (SIB) system within the voltage range for the intercalation reactions, and other  $NaMF_3$  materials (M = Co, Ni, Mn) have exhibited very low capacities ( $\sim 33 \text{ mAh}\cdot\text{g}^{-1}$ ) [22].

Nanostructuring with conductive materials can improve cell performance because it promotes: (i) a large surface area for effective contact with the electrolyte and low areal current density; (ii) facile diffusion of electrons/ions in the nanosized composite structure; (iii) homogeneous dispersion of nanosized particles on the conductive materials, which helps to lower the resistance between NCF and the current collector. Therefore, we synthesized NCF nanoclusters (NCs) that comprised NCF nanoparticles (NPs) homogeneously dispersed on the conductive surface of reduced graphene oxide (rGO). The rGO helps to electron transport between the current collector and NPs [26–28]. Moreover, NPs are well dispersed on rGO, because rGO has a large surface area and functional groups interacting with NPs [29–31]. The NCF NPs assembled to form NCs on the rGO and prevented self-aggregation of the NCF and rGO nanosheets [32].

Studies have reported the use of ball milling and roll-quenching processes for the preparation of nanosized  $NaMF_3$  [22,33,34]. However, the NPs formed using these methods are not uniformly sized. When the size of particles is not uniform, the active materials of the electrode layer show non-uniform reaction kinetics, resulting in low capacity under high current densities [35]. When the capacity of ball-milling synthesized  $NaFeF_3$  was tested in a SIB, the electrode delivered a capacity of  $169 \text{ mAh}\cdot\text{g}^{-1}$  in the potential range of 2–4.3 V [33]. However, it resulted in high charge/discharge polarization and poor cycle stability. In addition, NCF prepared by ball milling exhibits a rather low capacity of  $38 \text{ mAh}\cdot\text{g}^{-1}$  in the potential range from 2 to 4.6 V in SIBs. Dimov et al. also fabricated nanosized NCFs using the ball milling and roll-quenching method. However, they obtained a capacity of  $33 \text{ mAh}\cdot\text{g}^{-1}$  [22].

In this study, we synthesized NCF/rGO nanocomposites using a simple one-pot solvothermal process and investigated their electrochemical properties as cathodes for LIBs. A solvothermal process produces chemical compounds under high temperature and

pressure using ethylene glycol as the solvent, leading to making uniform NCs assembled by NPs under optimized synthetic conditions. The process has the advantage of achieving precise control over the particle sizes and high-purity NCF (almost no presence of measured impurities). Furthermore, the particles obtained from this method have a large surface area for  $\text{Li}^+$  insertion because 20 nm-sized NPs are gathered to form uniform spherical clusters with a diameter of 300–500 nm. The electrical conductivity of the synthesized NPs can be improved by synthesizing rGO composite structures. As a cathode material for LIBs, the NCF/rGO electrode exhibited a high specific capacity ( $465 \text{ mAh}\cdot\text{g}^{-1}$  at  $20 \text{ mA}\cdot\text{g}^{-1}$ ) through the conversion reaction. Additionally, the NCF/rGO electrode demonstrated a significantly higher capacity, which was five times the capacity of the electrode composed of bare NCF NCs.

## 2. Experimental

### 2.1. Synthesis of The NCF/rGO Nanocomposite

NCF/rGO nanocomposites were prepared by modifying a previously reported procedure [36]. First, GO (0.15 g) (Nanografi Co. Inc., Thuringia, Germany) was added in 40 mL of ethylene glycol (99.5%, Samchun Chemicals, Seoul, Korea) and dispersed using an ultrasonic liquid processor (VCX750, Sonics & Materials, Newtown, CT, USA). Ultrasonic dispersion was carried out for 30 min at 20 kHz with a nominal power of 750 W and 40% acoustic amplitude. In this process, jacketed beaker and cooling circulator were used to prevent overheating. Cobalt chloride hexahydrate ( $\text{CoCl}_2\cdot 6\text{H}_2\text{O}$ , 0.88 g) was dissolved separately in 20 mL of ethylene glycol using magnetic stirrer. Subsequently, the two solutions were mixed. Then, 0.2 g of trisodium citrate dihydrate ( $\text{Na}_3\text{Cit}$ ) and ammonium fluoride ( $\text{NH}_4\text{F}$ ) solution (0.411 g of  $\text{NH}_4\text{F}$  dissolved in 2 mL of distilled water) were added sequentially to the mixture and it was stirred for 30 min. Next, 1.2 g of sodium acetate ( $\text{NaOAc}$ ) was added under vigorous stirring. The resulting solution was transferred into a 100 mL Teflon-lined stainless-steel autoclave (JNT, Pohang, Korea). The autoclave was heated at  $200^\circ\text{C}$  for 12 h and then naturally cooled to room temperature. After heating treatment, the products were separated by centrifugation at 5000 rpm for 5 min and washed with ethyl alcohol several times. The washed products were dried at  $80^\circ\text{C}$  overnight. The synthesis method that was used to obtain the NCF NCs was similar to that used for the NCF/rGO nanocomposites, but GO-dispersed ethylene glycol was not used.

### 2.2. Materials Characterization

Powder X-ray diffraction (XRD) patterns were obtained using a Rigaku D/Max 2500/PC diffractometer (Rigaku Co., Tokyo, Japan) at a scanning rate of  $6.00^\circ\cdot\text{min}^{-1}$ . The morphologies of the materials were investigated using scanning electron microscopy (SEM; JSM-7000F, JEOL Ltd., Tokyo, Japan, acceleration voltage: 10.0 kV) and transmission electron microscopy (TEM; JEM-2000EX, JEOL Ltd., Tokyo, Japan, acceleration voltage: 200 kV). The Brunauer–Emmett–Teller (BET) surface area of the samples (Tristar II 3020, Micromeritics Inc., Norcross, GA, USA) was obtained from the nitrogen physisorption isotherms at 77 K. Pore size distributions were calculated from the adsorption branch of the isotherms using the Barrett–Joyner–Halenda (BJH) method. Raman spectroscopy was recorded on a Horiba Jobin-Yvon LabRam Aramis (Horiba, Kyoto, Japan) using laser excitation at 514 nm from an argon ion laser ( $<100 \mu\text{W}$ ,  $\times 50$ , and 300 s). Thermogravimetric analysis (TGA; Q600 SDT, TA instruments) was conducted at a heating rate of  $10^\circ\text{C}\cdot\text{min}^{-1}$  under airflow of  $100 \text{ mL}\cdot\text{min}^{-1}$ . The carbon content of the samples was determined by elemental analysis using a CS 744 carbon/sulfur analyzer (LECO Corporation, St. Joseph, MI, USA). X-ray absorption near-edge structure (XANES) spectra were collected from the BL10C beam line at the Pohang light source (PLS-II, Pohang, Korea).

### 2.3. Electrochemical Measurements

For electrode preparation, the NCF/rGO nanocomposite was mixed with super P carbon and polyvinylidene difluoride (PVDF) at a weight ratio of 8:1:1 in N-methyl-2-

pyrrolidone (NMP). The resulting slurry was coated onto an aluminum foil and dried at 100 °C in a vacuum. The dried electrodes were used to assemble coin cells (CR2032), using lithium foil as the counter and reference electrodes, and 1.0 M LiPF<sub>6</sub> in ethylene carbonate/dimethyl carbonate (EC/DMC; 1:1 volume ratio, Enchem Ltd., Jaechun, Korea) as the electrolyte. The galvanostatic charge/discharge analyses were conducted using a battery cycler (WBCS3000L, WonATech Co., Seoul, Korea) within a current rate range of 20–200 mA·g<sup>-1</sup>. The specific capacity and current rate calculations were based on the mass of NCF. Considering the mass ratio between NCF and rGO was 85:15, NCF control sample electrode was mixed with super P carbon and PVDF at a 7:2:1 ratio in NMP; the amount of super P carbon was controlled to obtain similar carbon contents in each electrode.

### 3. Results and Discussion

#### 3.1. Structural and Morphological Characterization

NCF/rGO nanocomposites were synthesized using the solvothermal process (Figure 1). CoCl<sub>2</sub>·6H<sub>2</sub>O (dissolved in ethylene glycol) and NH<sub>4</sub>F (dissolved in distilled water) were used as the cobalt and fluorine precursor solutions, respectively. Next, Na-containing precursors (NaOAc and Na<sub>3</sub>Cit, acting as the alkali source and electrostatic stabilizer) and graphene oxide were added to ethylene glycol. Na<sub>3</sub>Cit made NCF NCs uniformly shaped because of the strong coordination affinity of its multi-donating ligands with cobalt ions, which was consistent with previous reports [36,37]. In addition, an appropriate reaction temperature was crucial to obtain the NCF NCs of the target size without impurities during the solvothermal process [36]. The GO added to the solvothermal reaction was reduced to rGO using ethylene glycol as a solvent and reducing agent.

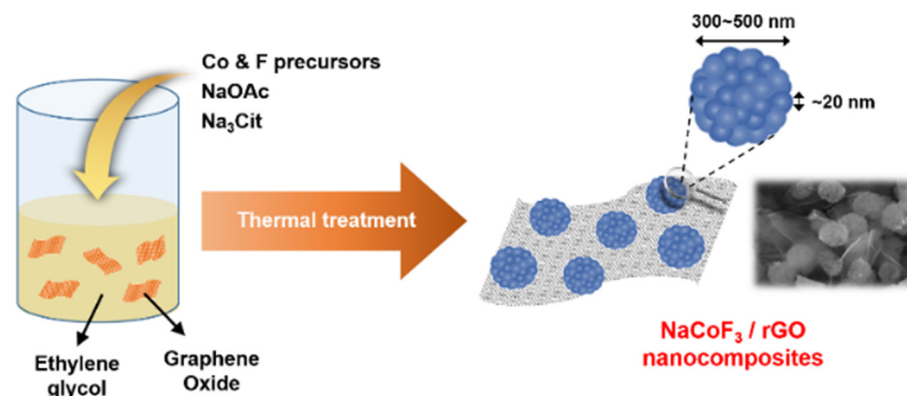
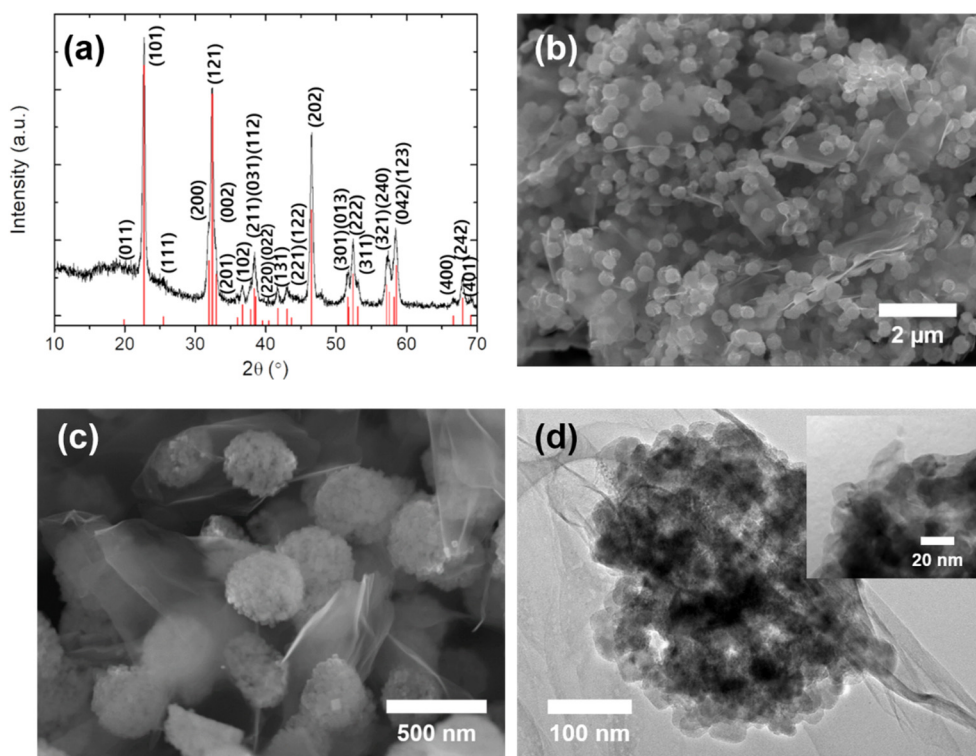


Figure 1. Schematic of the solvothermal synthesis of NCF/rGO nanocomposites.

NCF NCs were evenly distributed and combined with rGO, which may be explained as follows: (i) GO exhibits a quasi-two-dimensional carbon nanosheet structure with a high surface area. Hence, it can be used as a support material for loading of NCF NCs; (ii) the NCs were grown on the surface of graphene sheets owing to the interactions between the functional groups on the GO surface, such as carboxyl (-COOH) and hydroxyl (-OH) [38,39].

Figure 2a shows the XRD pattern of the NCF/rGO nanocomposites prepared by the solvothermal method. This pattern corresponds to a pure orthorhombic phase of NCF, which is consistent with the JCPDS card No. 70–1889. The diffraction peaks 2θ of 22.7, 32.3, 38.4, 46.5, 52.4, and 58.5° were assigned to (101), (121), (031), (202), (222), and (123), respectively. The average crystal size of these NPs was 17.6 ± 0.5 nm, as calculated by the Debye–Scherrer equation. The diffraction pattern of GO showed peaks at 2θ of approximately 9.6 and 19.4° (Figure S1a). For the NCF/rGO nanocomposites, these peaks disappeared and a broad peak located at approximately 20° was observed, indicating that GO was flaked and reduced. Impurity peaks corresponding to CoO<sub>x</sub>, NaF, and CoF<sub>2</sub> were not present (Figure 2a and Figure S1b).



**Figure 2.** (a) XRD pattern (red columns: the standard peaks of  $\text{NaCoF}_3$ , JCPDS No. 70-1889), (b,c) SEM images, and (d) TEM images of the NCF/rGO nanocomposites (inset: high-magnification the TEM image).

The morphology and size of the NCF/rGO nanocomposites were observed by SEM and TEM. The SEM images in Figure 2b,c illustrate the morphology of the NCF/rGO nanocomposites, comprised of uniform spherical NCF NCs (300–500 nm in diameter) and sheets of rGO. While NCF NCs maintained their original NCs structure (Figure S1c,d), the composites were evenly composed of rGO. As shown in the TEM images in Figure 2d, the NCF NCs, covered with rGO, were formed through the assembly of  $\sim 20$  nm NPs, which is almost the same as the crystallite size calculated by XRD. The large surface area of the NCs facilitated their contact with the electrolyte. Furthermore, NPs can react rapidly with electrons at an applied current, which improves ion diffusion by decreasing the solid-state ion diffusion distance. In addition, nanosized pores that were formed both inside the NCs (between each NP) and between the NCF NCs and rGO, stabilized the active material during the charge/discharge processes, during which large volume changes occur typically.

Raman spectroscopy analysis confirmed the reduction of GO to rGO during the solvothermal reaction (Figure 3a). The two samples exhibited large G and D-bands. The  $I_D/I_G$  intensity ratio increased from 0.92 (GO) to 1.05 (NCF/rGO). This difference explained the decrease in average size of the  $sp^2$  domain after reduction of the exfoliated GO and the removal of oxygen groups from the GO surface [40,41]. TGA and elemental analysis were performed to quantify the amount of rGO in the NCF/rGO nanocomposites (Figure S2). Excluding impurities, e.g., moisture, the weight ratio of NCF:rGO in the composite was estimated to be 85:15.

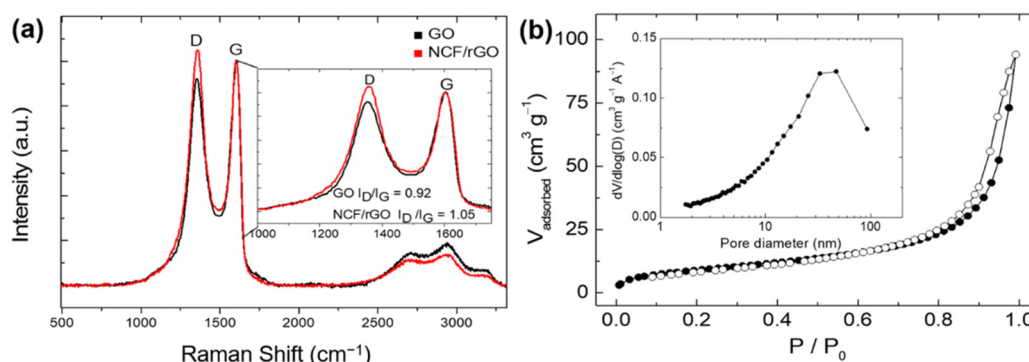


**Figure 3.** (a) Raman spectra of the GO and NCF/rGO samples; (b) Nitrogen physisorption isotherm and Barrett–Joyner–Halenda (BJH) pore size distribution (inset) of the NCF/rGO nanocomposite.

To investigate the surface area and pore volume of the NCF/rGO nanocomposite, we obtained nitrogen physisorption isotherms (Figure 3b). The surface area of the NCF/rGO nanocomposites was  $34 \text{ m}^2 \cdot \text{g}^{-1}$  as calculated by the BET method, and the pore volume of the NCF/rGO nanocomposite was  $0.146 \text{ cm}^3 \cdot \text{g}^{-1}$ . Nitrogen adsorption increased significantly from a  $P/P_0$  ratio of 0.9, indicating that a few tens of nanosized pores were formed. Further, Figure 3b (inset) shows the BJH pore size distribution. This broad pore size distribution corresponds to pores between the NCF NPs, those between the rGO sheets and the NCF NPs, and those between the rGO sheets. Moreover, nanosized pores can both improve the electrolyte wettability through capillary condensation and stabilize the electrode upon volume changes due to stress.

### 3.2. Electrochemical Performance

Figure S3a shows the galvanostatic charge/discharge profiles of the NCF/rGO nanocomposites obtained with 1 M  $\text{LiPF}_6$  in EC/DMC solution. The test was conducted to confirm whether desodiation ( $\text{NaCoF}_3 \leftrightarrow \text{Na}^+ + \text{CoF}_3$ ) was possible or not by increasing the voltage up to 5 V. The charge/discharge profile for NCF/rGO at 0.1 C, in the potential window of 2.5–5 V shows that a capacity of  $188 \text{ mAh} \cdot \text{g}^{-1}$  is obtained when the voltage was increased to 5 V in the first cycle. This capacity could be obtained (although there was no  $\text{Li}^+$  in the cathode) owing to the following reasons: (i) a desodiation reaction may have occurred; (ii) anions ( $\text{PF}_6^-$ ) would have influenced the capacity at the high-voltage range by adsorption on the rGO surface [42,43]; (iii) an irreversible electrolyte-decomposition reaction may have occurred. To confirm that desodiation hypothetically occurred, X-ray absorption spectroscopy was conducted to verify changes in the oxidation number of Co. XANES analysis in Figure S3b shows that the peak position of pristine NCF/rGO nanocomposites is measured at approximately 7725 eV. This was consistent with the peak positions of  $\text{Co}^{2+}$  that have been reported previously [44,45]. In addition, there was negligible change in the red line (after 5 V charging) and the black line (before the electrochemical reaction). This indicated that the oxidation number was unchanged and hence desodiation did not occur. This may be due to the structural stability of NCF. A higher voltage is required to induce desodiation, but it is difficult to achieve this using a commercial electrolyte. Therefore, the first charging capacity of  $188 \text{ mAh} \cdot \text{g}^{-1}$  was due to the irreversible electrolyte-decomposition reaction at high voltages. The first discharging capacity remarkably decreased to  $25 \text{ mAh} \cdot \text{g}^{-1}$ , which further supports the occurrence of the irreversible reaction process of NCF in the initial cycle.

Although desodiation did not occur, capacity due to a conversion reaction with  $\text{Li}^+$  can be obtained by decreasing the reaction operating voltage range. Figure 4 shows the charge/discharge profiles of the NCF/rGO nanocomposite electrode, measured in the potential range of 1–4.5 V at different current densities. In the first cycle, the specific capacity was  $514 \text{ mAh} \cdot \text{g}^{-1}$  at a discharge voltage (lithiation) of 1 V with a current density of  $20 \text{ mA} \cdot \text{g}^{-1}$ . A voltage plateau of less than 2 V was observed, which was similar to the

conversion reaction. Therefore, the conversion reaction of NCF occurred ( $2\text{Li}^+ + \text{NaCoF}_3 \leftrightarrow \text{Co} + 2\text{LiF} + \text{NaF}$ ) [46]. In the first cycle, a long voltage plateau was observed at 1.21 V. However, in the second discharge cycle, the voltage plateau reduced in length as the voltage increased. This indicated that the initial lithiation process led to the rearrangement of the atomic structures via the conversion reaction. Moreover, structural changes following the first conversion occurred during the first cycle. The first charge capacity of the NCF/rGO electrode was  $465 \text{ mAh}\cdot\text{g}^{-1}$  (initial coulombic efficiency of 90.5%). The reversible capacity of  $465 \text{ mAh}\cdot\text{g}^{-1}$  is the highest among the reported data for NCF in literature. At a current density of  $20 \text{ mA}\cdot\text{g}^{-1}$ , the capacity exceeded the theoretical capacity of NCF ( $385 \text{ mAh}\cdot\text{g}^{-1}$ ). This can be explained as follows: (i) additional  $\text{Li}^+$  might have been stored on the surface of rGO or anions ( $\text{PF}_6^-$ ) might have been adsorbed on the rGO surface [43]; (ii) owing to the nanosized particles, the corresponding surface area increased, resulting in interfacial  $\text{Li}^+$  insertion into the NCF NCs [47,48].

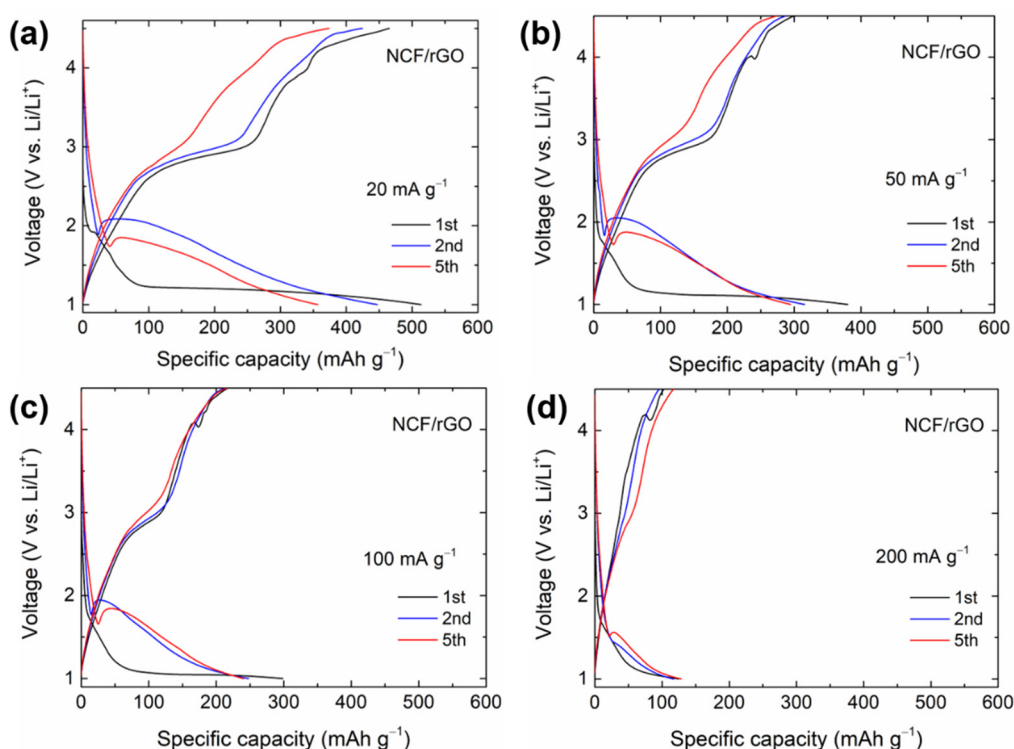


**Figure 4.** Galvanostatic charge/discharge curves of the 1st, 2nd, and 5th cycles for the NCF/rGO electrode at a current density of (a)  $20 \text{ mA}\cdot\text{g}^{-1}$ , (b)  $50 \text{ mA}\cdot\text{g}^{-1}$ , (c)  $100 \text{ mA}\cdot\text{g}^{-1}$ , and (d)  $200 \text{ mA}\cdot\text{g}^{-1}$ .

In the first cycle, the specific discharge capacity was measured to be 514, 363, 297, and  $119 \text{ mAh}\cdot\text{g}^{-1}$  at the current densities of 20, 50, 100, and  $200 \text{ mA}\cdot\text{g}^{-1}$ , respectively. NCF/rGO exhibited an initial discharge capacity of  $297 \text{ mAh}\cdot\text{g}^{-1}$  even at a current of  $100 \text{ mA}\cdot\text{g}^{-1}$ . This will be compared with the NCF electrode results.

As NCF has poor electrical conductivity, the NCF electrode (without the rGO supporting structure) could not achieve high capacities (Figure 5). In the first cycle, when the discharge voltage was 1 V, the specific capacities were 186, 139, 92, and  $11 \text{ mAh}\cdot\text{g}^{-1}$ , respectively, at different current densities (from 20 to  $200 \text{ mA}\cdot\text{g}^{-1}$ ). The reversible capacity of the NCF electrode was  $\sim 89 \text{ mAh}\cdot\text{g}^{-1}$  at  $20 \text{ mA}\cdot\text{g}^{-1}$ . As we confirmed in electrochemical analysis, although both electrodes have similar carbon content in the electrode layer, NCF/rGO electrode exhibited higher capacity ( $465 \text{ mAh}\cdot\text{g}^{-1}$  at  $20 \text{ mA}\cdot\text{g}^{-1}$ ), less polarization, and improved reversibility compared to those of NCF electrode. It can be inferred that rGO with highly dispersed 3-D structures played a crucial role in increasing the reversible capacities of the NCF electrodes owing to its high conductivity and enhanced contact with NCF NPs [49].

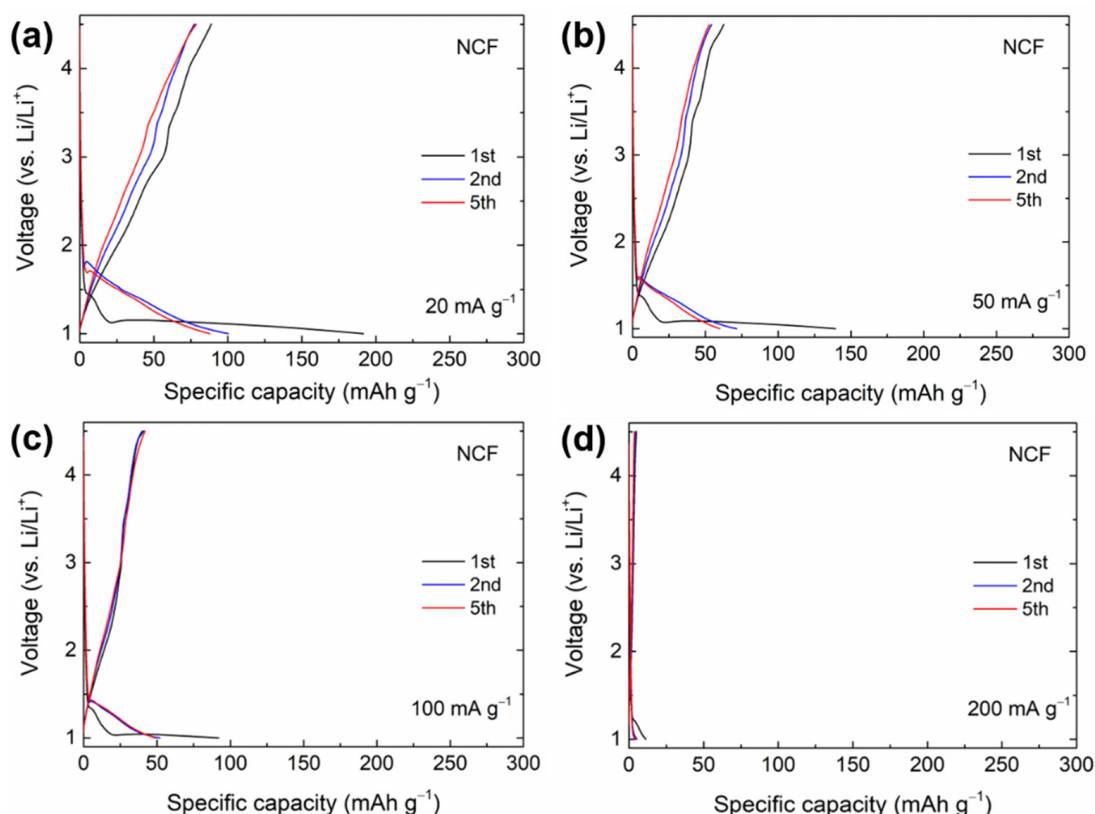


**Figure 5.** Galvanostatic charge/discharge curves of the 1st, 2nd, and 5th cycles for the NCF electrode at a current density of (a)  $20 \text{ mA}\cdot\text{g}^{-1}$  (b)  $50 \text{ mA}\cdot\text{g}^{-1}$  (c)  $100 \text{ mA}\cdot\text{g}^{-1}$ , and (d)  $200 \text{ mA}\cdot\text{g}^{-1}$ .

Figure 6 shows the cycling performance of the NCF/rGO and NCF electrodes at  $100 \text{ mA}\cdot\text{g}^{-1}$ . The NCF/rGO electrode exhibited higher capacities than the NCF electrode (without rGO) in all the cycles. The 50th cycle capacities of the NCF/rGO and NCF electrodes were  $111$  and  $24 \text{ mAh}\cdot\text{g}^{-1}$ , respectively. Although capacity reduction was observed for the NCF/rGO electrode, higher capacities were obtained, compared with the NCF electrode. Figure 7 shows the cycling performance of the cobalt fluoride-based materials at various current densities [22,50–55]. Interestingly, this is the first report showing promising cyclability of NCF. Moreover, NCF/rGO exhibits similar cyclability compared to some  $\text{CoF}_2$  cathodes. The capacity decrease observed for the NCF/rGO electrode can be attributed to Co dissolution at high voltages and stability decay due to changes in the particle structures during the conversion reaction [46,56]. In particular, as voltage increased during delithiation process, a portion of metallic Co is oxidized and easily dissolved as Co ions into the electrolyte [46]. Therefore, although the NCF/rGO electrode exhibited higher capacities than the practical capacities of commercial cathode materials, such as LCO ( $\sim 140 \text{ mAh}\cdot\text{g}^{-1}$ ) and NMC ( $160\text{--}200 \text{ mAh}\cdot\text{g}^{-1}$ ), at the initial stages, it is essential to improve the cyclability of NCF/rGO (cf. commercial cathode materials exhibit more than 80% capacity retention over hundreds of cycles). For future research, we can propose that the stability and thus the cell performance can be enhanced by introducing a fine coating layer on each NCF particle surface [57,58].

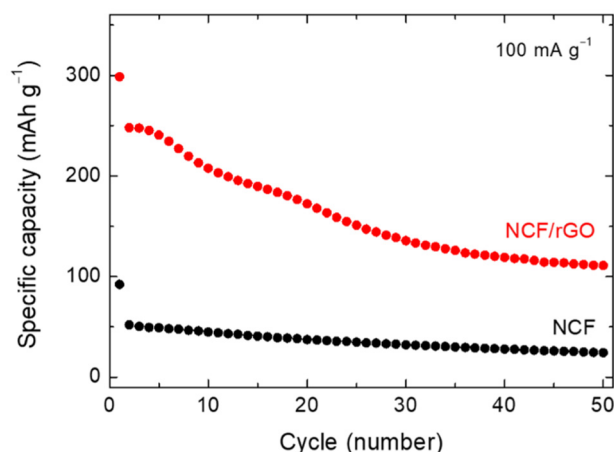


**Figure 6.** Cycling performance for the NCF/rGO and NCF electrodes at a current density of  $100 \text{ mA}\cdot\text{g}^{-1}$ .

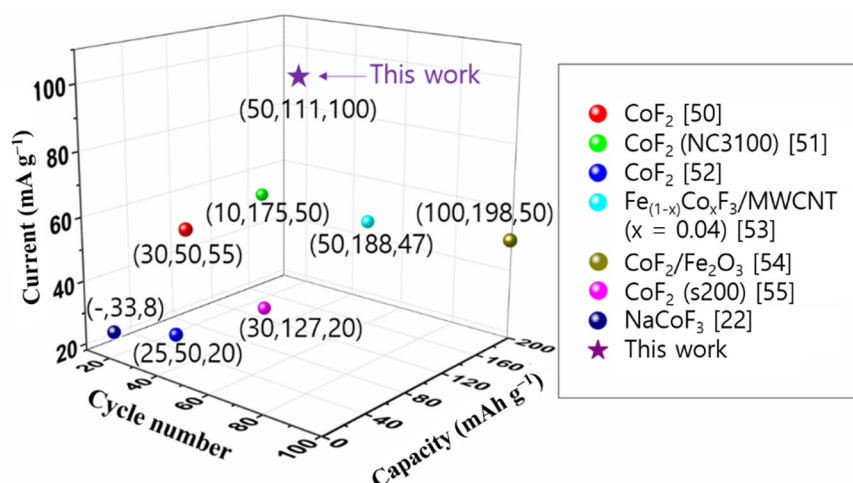


**Figure 7.** Cycle number vs capacity vs current of cobalt fluoride-based materials in LIB. The represented points are based on previous studies (x,y,z x: cycle number y: capacity, z: current).

#### 4. Conclusions

In summary, we synthesized NCF/rGO nanocomposites through a simple one-pot solvothermal process. The obtained NCF/rGO nanocomposites comprised 300–500 nm sized NCF NCs, which were assembled from NPs (~20 nm) incorporated on the surface of rGO (exhibiting excellent electrical conductivity). The nanosized particles resulted in a more efficient electrochemical reaction and enhanced ion diffusion. Moreover, through the uniform arrangement of the rGO sheets, NCF/rGO nanocomposites with high surface area ( $34 \text{ m}^2\cdot\text{g}^{-1}$ ) were obtained. As a cathode material for LIBs, the NCF/rGO electrode exhibited a high reversible capacity of  $465 \text{ mAh}\cdot\text{g}^{-1}$  at  $20 \text{ mA}\cdot\text{g}^{-1}$  in the conversion reaction, which is five times higher than the reversible capacity of the NCF electrode. Moreover, the NCF/rGO electrode exhibited enhanced specific capacity within the entire current density range ( $20\text{--}200 \text{ mA}\cdot\text{g}^{-1}$ ), compared with the performance of the NCF electrode. This study can contribute to metal fluoride research, demonstrating that this material can be a promising cathode for high energy density batteries.

**Supplementary Materials:** The following are available online at <https://www.mdpi.com/1996-1944/14/3/547/s1>, Figure S1: (a) XRD pattern of GO, (b) XRD pattern, (c) SEM image, and (d) TEM image of NCF NCs., Figure S2: Thermogravimetric analysis of NCF/rGO nanocomposites, Figure S3: (a) Galvanostatic charge/discharge curves of the 1st, 2nd and 3rd cycles of NCF/rGO at 0.1C, (b) X-ray absorption near edge structure (XANES) measurements of pristine and charged electrode.

**Author Contributions:** Conceptualization, J.C. and C.J.; methodology, C.J.; validation, J.C., C.J. and E.L.; formal analysis, J.O. and J.J.; investigation, J.O. and J.J.; resources, J.O. and J.J.; data curation, J.O. and J.J.; writing—original draft preparation, J.O. and J.J.; writing—review and editing, J.C., E.L. and C.J.; visualization, J.O. and J.J.; supervision, J.C., C.J. and E.L.; project administration, J.C., C.J. and E.L.; funding acquisition, J.C., C.J. and E.L. All authors have read and agreed to the published version of the manuscript.

**Funding:** This research was supported by the Chung-Ang University Graduate Research Scholarship in 2020 and conducted under the Competency Development Program for Industry Specialists of the Korean Ministry of Trade, Industry and Energy (MOTIE), operated by Korea Institute for Advancement of Technology (KIAT) (P0012453 Next-generation Display Expert Training Project for Innovation Process and Equipment, Materials Engineers). This research was further supported by the National Research Foundation of Korea (NRF) grant funded by the Korea government (MSIT) (2017R1C1B2005403).

**Institutional Review Board Statement:** Not applicable.

**Informed Consent Statement:** Not applicable.

**Data Availability Statement:** The data presented in this study are available on request from corresponding authors.

**Conflicts of Interest:** The authors declare no conflict of interest.

## References

1. Nayak, P.K.; Erickson, E.M.; Schipper, F.; Penki, T.R.; Munichandraiah, N.; Adelhelm, P.; Sclar, H.; Amalraj, F.; Markovsky, B.; Aurbach, D. Review on challenges and recent advances in the electrochemical performance of high capacity Li- and Mn-rich cathode materials for Li-ion batteries. *Adv. Energy Mater.* **2018**, *8*, 1702397. [[CrossRef](#)]
2. Kim, U.-H.; Park, G.-T.; Son, B.-K.; Nam, G.W.; Liu, J.; Kuo, L.-Y.; Kaghazchi, P.; Yoon, C.S.; Sun, Y.-K. Heuristic solution for achieving long-term cycle stability for Ni-rich layered cathodes at full depth of discharge. *Nat. Energy* **2020**, *5*, 860–869. [[CrossRef](#)]
3. Nitta, N.; Wu, F.; Lee, J.T.; Yushin, G. Li-ion battery materials: Present and future. *Mater. Today* **2015**, *18*, 252–264. [[CrossRef](#)]
4. Yi, T.-F.; Wei, T.-T.; Li, Y.; He, Y.-B.; Wang, Z.-B. Efforts on enhancing the Li-ion diffusion coefficient and electronic conductivity of titanate-based anode materials for advanced Li-ion batteries. *Energy Stor. Mater.* **2020**, *26*, 165–197. [[CrossRef](#)]
5. Foss, C.E.L.; Müssig, S.; Svensson, A.M.; Vie, P.J.S.; Ulvestad, A.; Mæhlen, J.P.; Kuposov, A.Y. Anodes for Li-ion batteries prepared from microcrystalline silicon and enabled by binder's chemistry and pseudo-self-healing. *Sci. Rep.* **2020**, *10*, 13193. [[CrossRef](#)] [[PubMed](#)]
6. Vorauer, T.; Kumar, P.; Berhaut, C.L.; Chamasemani, F.F.; Jouneau, P.-H.; Aradilla, D.; Tardif, S.; Pouget, S.; Fuchsbichler, B.; Helfen, L.; et al. Multi-scale quantification and modeling of aged nanostructured silicon-based composite anodes. *Commun. Chem.* **2020**, *3*, 141. [[CrossRef](#)]
7. Francis, C.F.J.; Kyratzis, I.L.; Best, A.S. Lithium-ion battery separators for ionic-liquid electrolytes: A review. *Adv. Mater.* **2020**, *32*, 1904205. [[CrossRef](#)]
8. Jang, J.; Oh, J.; Jeong, H.; Kang, W.; Jo, C. A review of functional separators for lithium metal battery applications. *Materials* **2020**, *13*, 4625. [[CrossRef](#)]
9. Wang, Q.; Jiang, L.; Yu, Y.; Sun, J. Progress of enhancing the safety of lithium ion battery from the electrolyte aspect. *Nano Energy* **2019**, *55*, 93–114. [[CrossRef](#)]
10. Hou, J.; Lu, L.; Wang, L.; Ohma, A.; Ren, D.; Feng, X.; Li, Y.; Li, Y.; Ootani, I.; Han, X.; et al. Thermal runaway of lithium-ion batteries employing LiN(SO<sub>2</sub>F)<sub>2</sub>-based concentrated electrolytes. *Nat. Commun.* **2020**, *11*, 5100. [[CrossRef](#)]
11. Ye, Y.; Chou, L.-Y.; Liu, Y.; Wang, H.; Lee, H.K.; Huang, W.; Wan, J.; Liu, K.; Zhou, G.; Yang, Y.; et al. Ultralight and fire-extinguishing current collectors for high-energy and high-safety lithium-ion batteries. *Nat. Energy* **2020**, *5*, 786–793. [[CrossRef](#)]
12. Tian, T.; Zhang, T.-W.; Yin, Y.-C.; Tan, Y.-H.; Song, Y.-H.; Lu, L.-L.; Yao, H.-B. Blow-spinning enabled precise doping and coating for improving high-voltage lithium cobalt oxide cathode performance. *Nano Lett.* **2020**, *20*, 677–685. [[CrossRef](#)] [[PubMed](#)]
13. Cho, J.; Kim, Y.J.; Park, B. Novel LiCoO<sub>2</sub> cathode material with Al<sub>2</sub>O<sub>3</sub> coating for a Li ion cell. *Chem. Mater.* **2000**, *12*, 3788–3791. [[CrossRef](#)]
14. Wu, F.; Borodin, O.; Yushin, G. In situ surface protection for enhancing stability and performance of conversion-type cathodes. *MRS Energy Sustain.* **2017**, *4*, E9. [[CrossRef](#)]
15. Wu, F.; Srot, V.; Chen, S.; Zhang, M.; van Aken, P.A.; Wang, Y.; Maier, J.; Yu, Y. Metal–Organic Framework-derived nanoconfinements of CoF<sub>2</sub> and mixed-conducting wiring for high-performance metal fluoride-lithium battery. *ACS Nano* **2020**. [[CrossRef](#)]
16. Liu, L.; Guo, H.; Zhou, M.; Wei, Q.; Yang, Z.; Shu, H.; Yang, X.; Tan, J.; Yan, Z.; Wang, X. A comparison among FeF<sub>3</sub>·3H<sub>2</sub>O, FeF<sub>3</sub>·0.33H<sub>2</sub>O and FeF<sub>3</sub> cathode materials for lithium ion batteries: Structural, electrochemical, and mechanism studies. *J. Power Sources* **2013**, *238*, 501–515. [[CrossRef](#)]

17. Wu, W.; Wang, X.; Wang, X.; Yang, S.; Liu, X.; Chen, Q. Effects of MoS<sub>2</sub> doping on the electrochemical performance of FeF<sub>3</sub> cathode materials for lithium-ion batteries. *Mater. Lett.* **2009**, *63*, 1788–1790. [[CrossRef](#)]
18. Zhang, W.; Ma, L.; Yue, H.; Yang, Y. Synthesis and characterization of in situ Fe<sub>2</sub>O<sub>3</sub>-coated FeF<sub>3</sub> cathode materials for rechargeable lithium batteries. *J. Mater. Chem.* **2012**, *22*, 24769–24775. [[CrossRef](#)]
19. Liu, L.; Zhou, M.; Yi, L.; Guo, H.; Tan, J.; Shu, H.; Yang, X.; Yang, Z.; Wang, X. Excellent cycle performance of Co-doped FeF<sub>3</sub>/C nanocomposite cathode material for lithium-ion batteries. *J. Mater. Chem.* **2012**, *22*, 17539–17550. [[CrossRef](#)]
20. Wang, F.; Robert, R.; Chernova, N.A.; Pereira, N.; Omenya, F.; Badway, F.; Hua, X.; Ruotolo, M.; Zhang, R.; Wu, L.; et al. Conversion Reaction Mechanisms in Lithium Ion Batteries: Study of the Binary Metal Fluoride Electrodes. *J. Am. Chem. Soc.* **2011**, *133*, 18828–18836. [[CrossRef](#)]
21. Badway, F.; Cosandey, F.; Pereira, N.; Amatucci, G.G. Carbon metal fluoride nanocomposites: High-capacity reversible metal fluoride conversion materials as rechargeable positive electrodes for Li batteries. *J. Electrochem. Soc.* **2003**, *150*, A1318. [[CrossRef](#)]
22. Dimov, N.; Nishimura, A.; Chihara, K.; Kitajou, A.; Gocheva, I.D.; Okada, S. Transition metal NaMF<sub>3</sub> compounds as model systems for studying the feasibility of ternary Li-M-F and Na-M-F single phases as cathodes for lithium-ion and sodium-ion batteries. *Electrochim. Acta* **2013**, *110*, 214–220. [[CrossRef](#)]
23. Zhou, X.; Sun, H.; Zhou, H.; Ding, J.; Xu, Z.; Bin, W.; Tang, J.; Yang, J. Enhancing the lithium storage capacity of FeF<sub>3</sub> cathode material by introducing C@LiF additive. *J. Electroanal. Chem.* **2018**, *810*, 41–47. [[CrossRef](#)]
24. Badway, F.; Pereira, N.; Cosandey, F.; Amatucci, G.G. Carbon-metal fluoride nanocomposites: Structure and electrochemistry of FeF<sub>3</sub>: C. *J. Electrochem. Soc.* **2003**, *150*, A1209. [[CrossRef](#)]
25. Zhou, M.; Zhao, L.; Kitajou, A.; Okada, S.; Yamaki, J.-i. Mechanism on exothermic heat of FeF<sub>3</sub> cathode in Li-ion batteries. *J. Power Sources* **2012**, *203*, 103–108. [[CrossRef](#)]
26. Karim, M.R.; Shinoda, H.; Nakai, M.; Hatakeyama, K.; Kamihata, H.; Matsui, T.; Taniguchi, T.; Koinuma, M.; Kuroiwa, K.; Kurmoo, M.; et al. Electrical conductivity and ferromagnetism in a reduced graphene–metal oxide hybrid. *Adv. Funct. Mater.* **2013**, *23*, 323–332. [[CrossRef](#)]
27. Pei, S.; Cheng, H.-M. The reduction of graphene oxide. *Carbon* **2012**, *50*, 3210–3228. [[CrossRef](#)]
28. Qu, B.; Ma, C.; Ji, G.; Xu, C.; Xu, J.; Meng, Y.S.; Wang, T.; Lee, J.Y. Layered SnS<sub>2</sub>-reduced graphene oxide composite—A high-capacity, high-rate, and long-cycle life sodium-ion battery anode material. *Adv. Mater.* **2014**, *26*, 3854–3859. [[CrossRef](#)]
29. Ali, G.; Oh, S.H.; Kim, S.Y.; Kim, J.Y.; Cho, B.W.; Chung, K.Y. An open-framework iron fluoride and reduced graphene oxide nanocomposite as a high-capacity cathode material for Na-ion batteries. *J. Mater. Chem. A* **2015**, *3*, 10258–10266. [[CrossRef](#)]
30. Yu, S.-H.; Conte, D.E.; Baek, S.; Lee, D.-C.; Park, S.-K.; Lee, K.J.; Piao, Y.; Sung, Y.-E.; Pinna, N. Structure-properties relationship in iron oxide-reduced graphene oxide nanostructures for Li-ion batteries. *Adv. Funct. Mater.* **2013**, *23*, 4293–4305. [[CrossRef](#)]
31. Zhu, X.; Zhu, Y.; Murali, S.; Stoller, M.D.; Ruoff, R.S. Nanostructured reduced graphene oxide/Fe<sub>2</sub>O<sub>3</sub> composite as a high-performance anode material for lithium ion batteries. *ACS Nano* **2011**, *5*, 3333–3338. [[CrossRef](#)] [[PubMed](#)]
32. Li, Z.; Deng, S.; Xu, R.; Wei, L.; Su, X.; Wu, M. Combination of nitrogen-doped graphene with MoS<sub>2</sub> nanoclusters for improved Li-S battery cathode: Synthetic effect between 2D components. *Electrochim. Acta* **2017**, *252*, 200–207.
33. Kitajou, A.; Ishado, Y.; Yamashita, T.; Momida, H.; Oguchi, T.; Okada, S. Cathode properties of perovskite-type NaMF<sub>3</sub> (M=Fe, Mn, and Co) prepared by mechanical ball milling for sodium-ion battery. *Electrochim. Acta* **2017**, *245*, 424–429. [[CrossRef](#)]
34. Kitajou, A.; Komatsu, H.; Nagano, R.; Okada, S. Synthesis of FeOF using roll-quenching method and the cathode properties for lithium-ion battery. *J. Power Sources* **2013**, *243*, 494–498. [[CrossRef](#)]
35. Yoo, S.; Kang, B. Inhomogeneous delithiation behavior of chemically delithiated Li<sub>0.49</sub>FePO<sub>4</sub> particles of different sizes using a simple centrifuge separation method. *Electrochim. Acta.* **2015**, *151*, 270–275. [[CrossRef](#)]
36. Chun, J.; Jo, C.; Lim, E.; Roh, K.C.; Lee, J. Solvothermal synthesis of sodium cobalt fluoride (NaCoF<sub>3</sub>) nanoparticle clusters. *Mater. Lett.* **2017**, *207*, 89–92. [[CrossRef](#)]
37. Hwang, J.; Chun, J. Microwave-assisted solvothermal synthesis of sodium metal fluoride (Na<sub>x</sub>MF<sub>y</sub>) nanopowders. *J. Am. Ceram* **2019**, *102*, 6475–6479. [[CrossRef](#)]
38. Papiya, F.; Nandy, A.; Mondal, S.; Kundu, P.P. Co/Al<sub>2</sub>O<sub>3</sub>-rGO nanocomposite as cathode electrocatalyst for superior oxygen reduction in microbial fuel cell applications: The effect of nanocomposite composition. *Electrochim. Acta* **2017**, *254*, 1–13.
39. Ji, Z.; Wang, Y.; Yang, J.; Shen, X.; Yu, Q.; Kong, L.; Zhou, H. Reduced graphene oxide uniformly decorated with Co nanoparticles: Facile synthesis, magnetic and catalytic properties. *RSC Adv.* **2016**, *6*, 107709–107716.
40. Stankovich, S.; Dikin, D.A.; Piner, R.D.; Kohlhaas, K.A.; Kleinhammes, A.; Jia, Y.; Wu, Y.; Nguyen, S.T.; Ruoff, R.S. Synthesis of graphene-based nanosheets via chemical reduction of exfoliated graphite oxide. *Carbon* **2007**, *45*, 1558–1565.
41. Loryuenyong, V.; Totepvimarn, K.; Eimburanaprat, P.; Boonchompoo, W.; Buasri, A. Preparation and characterization of reduced graphene oxide sheets via water-based exfoliation and reduction methods. *Adv. Mater. Sci. Eng.* **2013**, *2013*, 923403. [[CrossRef](#)]
42. Qi, X.; Blizanac, B.; DuPasquier, A.; Meister, P.; Placke, T.; Oljaca, M.; Li, J.; Winter, M. Investigation of PF<sub>6</sub><sup>−</sup> and TFSI<sup>−</sup> anion intercalation into graphitized carbon blacks and its influence on high voltage lithium ion batteries. *Phys. Chem. Chem. Phys.* **2014**, *16*, 25306–25313. [[CrossRef](#)] [[PubMed](#)]
43. Miyoshi, S.; Akbay, T.; Kurihara, T.; Fukuda, T.; Staykov, A.T.; Ida, S.; Ishihara, T. Fast diffusivity of PF<sub>6</sub><sup>−</sup> anions in graphitic carbon for a dual-carbon rechargeable battery with superior rate property. *J. Mater. Chem. C* **2016**, *120*, 22887–22894. [[CrossRef](#)]

44. Fu, X.-P.; Shen, Q.-K.; Shi, D.; Wu, K.; Jin, Z.; Wang, X.; Si, R.; Song, Q.-S.; Jia, C.-J.; Yan, C.-H.  $\text{Co}_3\text{O}_4\text{-Al}_2\text{O}_3$  mesoporous hollow spheres as efficient catalyst for Fischer-Tropsch synthesis. *Appl. Catal. B* **2017**, *211*, 176–187. [[CrossRef](#)]
45. Hunault, M.; Robert, J.L.; Newville, M.; Galois, L.; Calas, G. Spectroscopic properties of five-coordinated  $\text{Co}^{2+}$  in phosphates. *SAA* **2014**, *117*, 406–412. [[CrossRef](#)]
46. Chun, J.; Jo, C.; Sahgong, S.; Kim, M.G.; Lim, E.; Kim, D.H.; Hwang, J.; Kang, E.; Ryu, K.A.; Jung, Y.S.; et al. Ammonium fluoride mediated synthesis of anhydrous metal fluoride–mesoporous carbon nanocomposites for high-performance lithium ion battery cathodes. *ACS Appl. Mater. Interfaces* **2016**, *8*, 35180–35190. [[CrossRef](#)]
47. Zhukovskii, Y.F.; Kotomin, E.A.; Balaya, P.; Maier, J. Enhanced interfacial lithium storage in nanocomposites of transition metals with  $\text{LiF}$  and  $\text{Li}_2\text{O}$ : Comparison of DFT calculations and experimental studies. *Solid State Sci.* **2008**, *10*, 491–495. [[CrossRef](#)]
48. Wang, Y.; Huang, Z.X.; Shi, Y.; Wong, J.I.; Ding, M.; Yang, H.Y. Designed hybrid nanostructure with catalytic effect: Beyond the theoretical capacity of  $\text{SnO}_2$  anode material for lithium ion batteries. *Sci. Rep.* **2015**, *5*, 9164. [[CrossRef](#)]
49. Fan, X.; Zhu, Y.; Luo, C.; Gao, T.; Suo, L.; Liou, S.-C.; Xu, K.; Wang, C. In situ lithiated  $\text{FeF}_3/\text{C}$  nanocomposite as high energy conversion-reaction cathode for lithium-ion batteries. *J. Power Sources* **2016**, *307*, 435–442. [[CrossRef](#)]
50. Tan, J.; Liu, L.; Guo, S.; Hu, H.; Yan, Z.; Zhou, Q.; Huang, Z.; Shu, H.; Yang, X.; Wang, X. The electrochemical performance and mechanism of cobalt (II) fluoride as anode material for lithium and sodium ion batteries. *Electrochim. Acta* **2015**, *168*, 225–233. [[CrossRef](#)]
51. Teng, Y.T.; Pramana, S.S.; Ding, J.; Wu, T.; Yazami, R. Investigation of the conversion mechanism of nanosized  $\text{CoF}_2$ . *Electrochim. Acta* **2013**, *107*, 301–312. [[CrossRef](#)]
52. Armstrong, M.J.; Panneerselvam, A.; O'Regan, C.; Morris, M.A.; Holmes, J.D. Supercritical-fluid synthesis of  $\text{FeF}_2$  and  $\text{CoF}_2$  Li-ion conversion materials. *J. Mater. Chem. A* **2013**, *1*, 10667–10676. [[CrossRef](#)]
53. Li, J.; Xu, S.; Huang, S.; Lu, L.; Lan, L.; Li, S. In situ synthesis of  $\text{Fe}_{(1-x)}\text{Co}_x\text{F}_3/\text{MWCNT}$  nanocomposites with excellent electrochemical performance for lithium-ion batteries. *J. Mater. Sci.* **2018**, *53*, 2697–2708. [[CrossRef](#)]
54. Cheng, Q.; Chen, Y.; Lin, X.; Liu, J.; Yuan, Z.; Cai, Y. Hybrid cobalt(II) fluoride derived from a bimetallic zeolitic imidazolate framework as a high-performance cathode for lithium-ion batteries. *J. Phys. Chem. C* **2020**, *124*, 8624–8632. [[CrossRef](#)]
55. Guan, Q.; Cheng, J.; Li, X.; Ni, W.; Wang, B. Porous  $\text{CoF}_2$  spheres synthesized by a one-pot solvothermal method as high capacity cathode materials for lithium-ion batteries. *Chin. J. Chem.* **2017**, *35*, 48–54. [[CrossRef](#)]
56. Senoh, H.; Matsui, K.; Shikano, M.; Okumura, T.; Kiuchi, H.; Shimoda, K.; Yamanaka, K.; Ohta, T.; Fukunaga, T.; Sakaebe, H.; et al. Degradation mechanism of conversion-type iron trifluoride: Toward improvement of cycle performance. *ACS Appl. Mater. Interfaces* **2019**, *11*, 30959–30967. [[CrossRef](#)]
57. Li, C.; Zhang, H.P.; Fu, L.J.; Liu, H.; Wu, Y.P.; Rahm, E.; Holze, R.; Wu, H.Q. Cathode materials modified by surface coating for lithium ion batteries. *Electrochim. Acta* **2006**, *51*, 3872–3883. [[CrossRef](#)]
58. Chen, Z.; Qin, Y.; Amine, K.; Sun, Y.K. Role of surface coating on cathode materials for lithium-ion batteries. *J. Mater. Chem.* **2010**, *20*, 7606–7612. [[CrossRef](#)]